Design and Ground Verification for Vision-Based Relative Navigation Systems of Microsatellites

DU Ronghua[1*], *LIAO Wenhe*[2], *ZHANG Xiang*[2]

1. School of Aviation Manufacturing and Mechanical Engineering, Nanchang Hangkong University,
Nanchang 330063, P. R. China;
2. Micro/Nano Satellite Research Center, Nanjing University of Science and Technology, Nanjing 210094, P. R. China

(Received 4 September 2024; revised 22 January 2025; accepted 12 February 2025)

Abstract: This paper presents the design and ground verification for vision-based relative navigation systems of microsatellites, which offers a comprehensive hardware design solution and a robust experimental verification methodology for practical implementation of vision-based navigation technology on the microsatellite platform. Firstly, a low power consumption, light weight, and high performance vision-based relative navigation optical sensor is designed. Subsequently, a set of ground verification system is designed for the hardware-in-the-loop testing of the vision-based relative navigation systems. Finally, the designed vision-based relative navigation optical sensor and the proposed angles-only navigation algorithms are tested on the ground verification system. The results verify that the optical simulator after geometrical calibration can meet the requirements of the hardware-in-the-loop testing of vision-based relative navigation systems. Based on experimental results, the relative position accuracy of the angles-only navigation filter at terminal time is increased by 25.5%, and the relative speed accuracy is increased by 31.3% compared with those of optical simulator before geometrical calibration.

Key words: microsatellites; vision-based relative navigation; optical simulator; ground verification; angles-only navigation

CLC number: V249.32 **Document code:** A **Article ID:** 1005-1120(2025)01-0037-19

0 Introduction

With the continuous development of space technology in various countries around the world, the application of spacecraft has become diversified. The scope of space missions is no longer limited to traditional applications such as communications, navigation, and remote sensing, but has expanded to civil aerospace and military missions, including space debris removal[1-2], on-orbit servicing[3-4], on-orbit assembly[5], formation flying[6-7], deep space exploration[8-9], and space attack and defense[10]. Such missions have emerged as popular areas of research in the field of spacecraft, and related techniques have emerged as leading-edge technologies in global competition. To meet the demands of missions that call for cost-effective and timely development solutions, traditional satellites have been found to be prohibitively expensive and time-consuming to develop. By contrast, microsatellites offer advantages such as compact size, low weight, reduced power consumption, shorter development cycles, high performance-to-price ratio, and high functional density.

In the aforementioned space missions, there are higher requirements for the mission capability of the microsatellite platform, and the autonomous operation capability needs to be urgently improved. Notably, such space missions typically involve gradually approaching a non-cooperative target space-

---

*Corresponding author, E-mail address: 71301@nchu.edu.cn.

How to cite this article: DU Ronghua, LIAO Wenhe, ZHANG Xiang. Design and ground verification for vision-based relative navigation systems of microsatellites[J]. Transactions of Nanjing University of Aeronautics and Astronautics, 2025, 42(1):37-55.

http://dx.doi.org/10.16356/j.1005-1120.2025.01.003

craft from a distance. As a result, the relative navigation system of spacecraft is subject to increasingly stringent requirements. The core capability of the microsatellite platform is that an observation spacecraft should have the ability of autonomous navigation, autonomous guidance and control to achieve autonomous proximity to a non-cooperative target spacecraft in space. So far, the traditional measurement method for the spacecraft autonomous rendezvous and docking missions involves combining multiple sensors such as microwave radar, laser radar, relative global position system (GPS), and optical camera to complete all relative navigation tasks in a segmented manner[11]. Owing to the relative navigation system composed of such sensors being considerably complex and expensive, the application of such navigation mode in autonomous proximity operation missions with a non-cooperative target spacecraft based on the microsatellite platform is largely limited. Thus, the study of autonomous relative navigation with small size, low cost, and high performance is the essential enabling technology for conducting autonomous proximity operations with a non-cooperative target spacecraft using the microsatellite platform. The vision-based relative navigation method is a relatively low-cost option because passive sensors are used for relative measurement, especially passive optical cameras, which have exhibited advantages in such space missions[12-15]. Passive optical cameras can easily obtain the line-of-sight vectors relative to the target spacecraft, and perform relative navigation operations according to these obtained line-of-sight vectors[16], which is also known as the angles-only navigation technology.

Before applying the vision-based relative navigation technology to the real spacecraft on-orbit missions, a large number of ground verification experiments need to be conducted. Since in-orbit flight experiments of real spacecraft are difficult and costly, the ground verification technology can provide the optimal method for the testing and verification of spacecraft, and allow for comprehensive testing and verification of the whole spacecraft system to be conducted without any physical flight. Moreover, most of the existing research methods on the vision-based relative navigation technology focus on numerical simulation[17-24], and there has been little research conducted on ground-based hardware-in-the-loop testing of the vision-based relative navigation systems for gradually approaching a target spacecraft from a distance (i.e., the longest distance is dozens of kilometers away, and the nearest distance is to docking). Furthermore, some studies only focus on hardware-in-the-loop testing of vision-based relative navigation systems at close range. As a result, this area of study holds significant research value.

In consideration of the aforementioned problems, in-depth research on the ground verification technology of the hardware-in-the-loop testing of the vision-based relative navigation systems is conducted in the present study, so as to provide an effective experimental method and a system-wide hardware design solution for the engineering application of the vision-based relative navigation technology on the microsatellite platform. The present paper is organized as follows: The detailed design of the vision-based relative navigation optical sensor is introduced in Section 1; the detailed design of the ground verification system for the hardware-in-the-loop testing of the vision-based relative navigation systems is provided in Section 2; a discussion on the hardware-in-the-loop testing, the result analysis for the vision-based relative navigation optical sensor and the proposed angles-only navigation algorithms are given in Section 3; and conclusions of the study are provided in Section 4.

1 Optical Sensor Design

The main function of the vision-based relative navigation optical sensor is to image the target spacecraft, accomplish the autonomous recognition and tracking of the target spacecraft in the images, and output line-of-sight vectors of the target spacecraft relative to the vision-based relative navigation optical sensor. The detailed design of the vision-based relative navigation optical sensor is described in this section. Considering the limitations of the size, weight, and power consumption of the microsatellite platform, a low power consumption, light weight, and high performance vision-based relative navigation optical sensor that can be applied to the microsatellite platform is successfully designed, thereby laying a solid foundation for the engineering application of the vision-based relative navigation technology on the microsatellite platform.

1.1 Hardware composition

The vision-based relative navigation optical sensor is designed with a large numerical aperture and a small field of view, thereby improving the dynamic range of the optical sensor, and eliminating the stray light inside and outside the field of view through a special lens hood, so as to improve the imaging quality of the vision-based relative navigation optical sensor. As shown in Fig.1, the vision-based relative navigation optical sensor is composed of an imaging lens, a lens hood, an electronic warehouse, an imaging circuit board, and an image acquisition and processing circuit board. In terms of structural design, a multi-layer mechanical structure is adopted for the vision-based relative navigation optical sensor, which allows for all components to be compactly assembled together, minimizing the volume and weight of the vision-based relative navigation optical sensor, so as to meet the requirements of the microsatellite platform. Table 1 shows the performance parameter design of the vision-based relative navigation optical sensor.

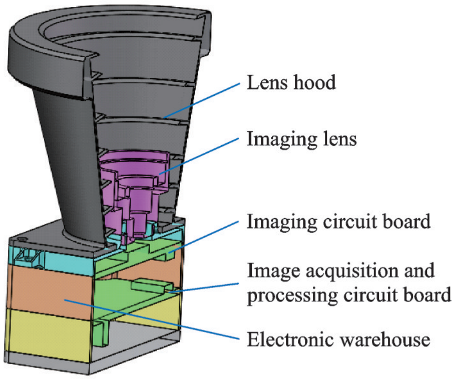

(a) Three-dimensional model

(b) Physical image

Fig.1 Vision-based relative navigation optical sensor

Table 1 Performance parameter design of the optical sensor

Parameter	Value
Focal length/mm	25
Resolution	1 280×1 024
Field angle/(°)	15×12
Frame frequency/(f•s^{-1})	≥30
Power consumption/W	≤2
Envelope size/(mm×mm×mm)	50×50×90
Mass/g	<160
Sensitive magnitude	6 magnitude
Use distance range	100 m—50 km

The main function of the vision-based relative navigation optical sensor is to image and recognize the target spacecraft. Firstly, the optical signal including the target spacecraft and the background enters the lens hood, thereby eliminating the stray light inside and outside the field of view, and improving the quality of the effective optical signal entering the optical sensor. Subsequently, the imaging lens focuses the optical signal in the field of view on the imaging sensor, which converts the optical signal into the analog electrical signal through photoelectric conversion. The analog electrical signal is then converted and subsequently collected, following which a digital signal that describes the image information is obtained through digital-to-analog conversion. The digital signal is then processed to determine the area of the target spacecraft within the images. Such processing also yields the line-of-sight vectors of the target spacecraft relative to the vision-based relative navigation optical sensor. Finally, the line-of-sight vectors are output to the guidance navigation and control (GNC) computer through the appropriate electrical interface (i.e., RS422/RS232).

The interface design of the vision-based relative navigation optical sensor is shown in Fig.2. The connector J30V2_25TJN-P3 is an external input and output interface, including power supply, JTAG program debugging, RS422/RS232 interface, and GND pins.

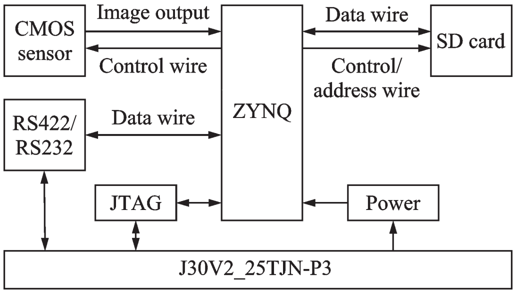

Fig.2 Interface design of the optical sensor

1.2 Imaging lens design

The main function of the imaging lens is to focus the optical signal in the field of view on the CMOS sensor, so as to image the target spacecraft on the photosensitive surface of the CMOS sensor. The imaging lens of the vision-based relative navigation optical sensor designed in the present study not only needs to meet the requirements of small distortion to improve the centroid positioning accuracy of the target spacecraft in images, but also needs to ensure a higher single-pixel energy concentration in the full field of view. Finally, the performance parameters of the designed imaging lens are shown in Table 2. Fig.3 shows the modulation transfer function (MTF) curves of the imaging lens, and Fig.4 shows the distortion curves of the imaging lens. An observation can be made from Figs.3—4 that the full-field MTF of the imaging lens is found to be better than 0.6@46 lp/mm, and the full-field distortion is less than 0.1%.

Table 2 Performance parameters of the imaging lens

Parameter	Value
Focal length/mm	25
Full-field distortion	$<0.1\%$
Full-field distortion	$<0.1\%$
MTF	$\geqslant$0.6@46 lp/mm
F number	2.8

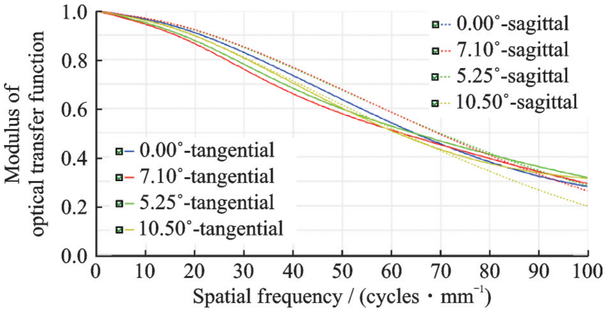

Fig.3 MTF curves of the imaging lens

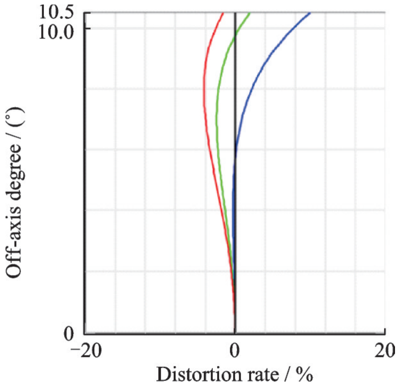

Fig.4 Distortion curves of the imaging lens

1.3 Lens hood design

Due to the extremely weak sunlight reflection from a target spacecraft at a long distance, coupled with the highly complex illumination environment in space, the vision-based relative navigation optical sensor is susceptible to interference from various sources. Such sources include sun stray light, ground-air stray light, and system internal stray light[25]. Moreover, a lens hood needs to be added to eliminate the impact of the stray light. Stray light entering the optical system through the inlet end of the lens hood undergoes only one attenuation, which occurs during reflection on the inner wall of the lens hood. As a result, the current design of the lens hood does not meet the required design specifications. It is therefore necessary to enhance the lens hood's ability to suppress stray light. Typically, this is accomplished by incorporating a light barrier on the inner wall of the lens hood. Finally, the inner wall of the designed lens hood has a hyperbola and parabola shaped light barrier, and a new type of adaptive low-stray light conical lens hood is designed. Fig.5 shows the three-dimensional model of the lens hood. Through the point source transmittance (PST) performance testing, findings are made that the low-stray light conical lens hood has good ability to eliminate stray light. When the off-axis angle exceeds 10°, the PST magnitude drops to below 10^{-6}. Additionally, the low-stray light conical lens hood effectively suppresses sun stray light up to an angle greater than 25°, and ground-air stray light up to an angle greater than 20°.

Fig.5 Low-stray light conical lens hood

1.4 Electronic warehouse design

A multi-layer mechanical structure is adopted for the electronic warehouse of the vision-based relative navigation optical sensor, which allows for all components to be compactly assembled together, minimizing the volume and weight of the vision-based relative navigation optical sensor. The electronic warehouse of the vision-based relative navigation optical sensor designed in the present study consists of four parts, including the upper end cover, the middle first layer, the middle second layer, and the bottom end cover. The upper end cover is mechanically connected with the imaging lens. The imaging circuit board is placed on the middle first layer, and the image acquisition and processing circuit board is placed on the middle second layer. The lens hood, the bottom end cover, the middle first layer, the middle second layer, and the upper end cover are fixedly connected with nuts through four M2.5 long screws. The entire electronic warehouse of the vision-based relative navigation optical sensor is constructed from AL6061 material and has undergone black anodizing treatment. Fig.6 depicts the three-dimensional model and physical image of the electronic warehouse.

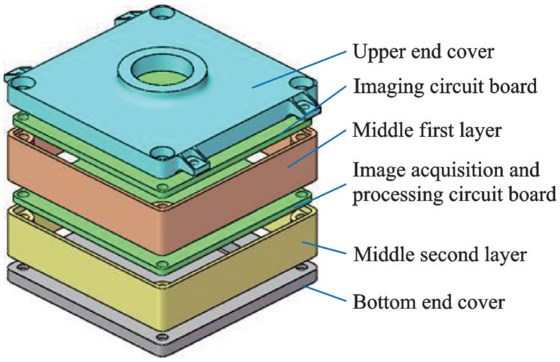

(a) Three-dimensional model

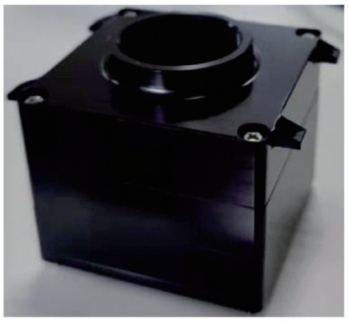

(b) Physical image

Fig.6 Electronic warehouse of the optical sensor

1.5 Imaging circuit board design

At present, the commonly used image sensors include CCD and CMOS, both of which use photodiodes for photoelectric conversion. CCD image sensor is a type of charge-coupled device, which belongs to the relatively early and mature imaging device. CMOS refers to the complementary metal oxide semiconductor, which is a voltage controlled amplification device and the basic unit of CMOS digital integrated circuit. In the field of digital imaging, the CMOS image sensor has emerged as a cost-effective alternative to traditional photosensitive components. In comparison to the CCD image sensor, the CMOS image sensor boasts several advantages, including superior imaging quality, high levels of integration, fast readout rates, and low power consumption. Thus, the CMOS image sensor e2v EV76C660 is selected as the imaging device for the imaging circuit board designed in the present study, owing to the high spectral response efficiency and ability to perform high frame rate imaging. Table 3 shows the performance parameters of the EV76C660 chip, and Fig.7 shows the spectral response curves of the EV76C660 chip. It can be seen from Fig.7 that the spectral response range and efficiency of the

EV76C660 chip are relatively high, fully meeting the requirements for use.

Table 3 Performance parameters of the EV76C660 chip

Parameter	Value
Number of effective pixels	1 280×1 024
Image size/(″)	1/1.8
Frame frequency/(f•s^{-1})	≤60
Bit depth/b	10
Pixel size/(μm×μm)	5.3×5.3
Pixel frequency/(Mpixels•s^{-1})	90—120
Temperature range/℃	−30—+60
Power consumption/mW	<200

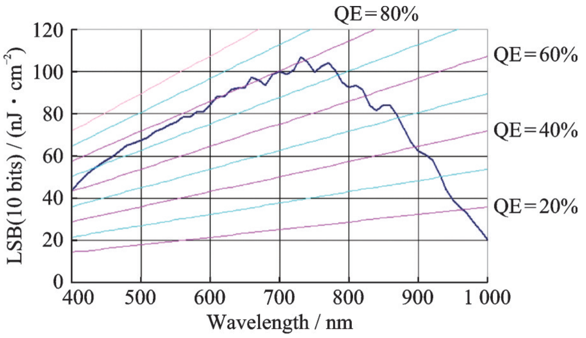

Fig.7 Spectral response curves of the EV76C660 chip

As depicted in Fig.8, the imaging circuit board contains the necessary peripheral circuit to facilitate the normal operation of the EV76C660 chip, as well as an interface circuit for external input and output. The primary function is to supply the EV76C660 chip with starting voltage, drive the chip to convert the optical signal into an analog electrical signal, and transmit it to the image acquisition and processing circuit board. An observation can be made from Fig.8 that the peripheral circuit provides starting voltages of 3.3 V and 1.8 V, as well as a reference clock, to the EV76C660 chip. Such voltages are generated using the 5 V power supply connected to the image acquisition and processing circuit board, with the LT1963ES8 chip serving as the voltage converter. Moreover, the image acquisition and processing circuit board configures registers in the EV76C660 chip through SPI protocol, so that parameters of the EV76C660 chip in the process of photoelectric conversion can be changed. Since the analog electrical signal voltage (1.8 V) obtained after the conversion of EV76C660 chip does not match the pin voltage (3.3 V) of ZYNQ chip, SN74AVC8T24 chip is selected as the level converter for the signal interaction between EV76C660 chip and ZYNQ chip. The hardware design of the imaging circuit board is shown in Fig.9, which shows the arrangement of components of the imaging circuit board.

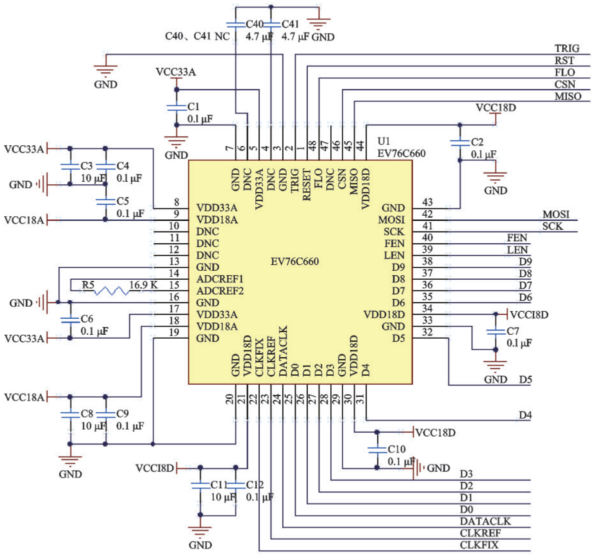

Fig.8 Peripheral circuit of the EV76C660 chip

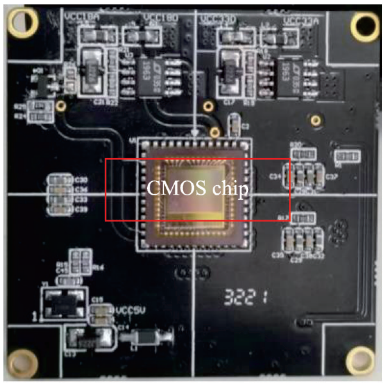

(a) Front

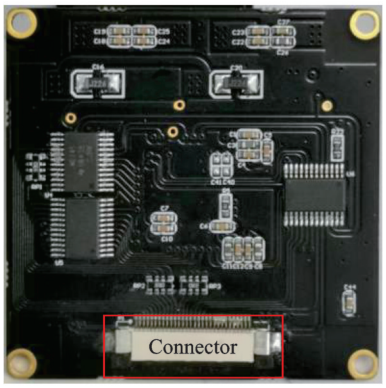

(b) Back

Fig.9 Hardware design of the imaging circuit board

1.6 Image acquisition and processing circuit board design

The primary function of the image acquisition and processing circuit board is to collect the analog electrical signal generated by the imaging circuit board, and convert it into a digital signal that represents the image information. The digital signal is then processed to determine the area of the target spacecraft in images, and the line-of-sight vectors of the target spacecraft relative to the vision-based relative navigation optical sensor are calculated. Finally, the line-of-sight vectors are output to the GNC computer through the RS422/RS232 interface.

For the image acquisition and processing circuit board, the ZYNQ XC7Z035-FFG676-2I chip (Kinex-7 architecture) is selected as the main processor. The ZYNQ XC7Z035-FFG676-2I chip integrates ARM Cortex-A9 dual-core CPU with a working frequency of 800 MHz. The ZYNQ XC7Z035-FFG676-2I chip offers two system clock options, namely a 100 MHz clock to the PL terminal and a 33.333 MHz clock to the PS terminal. The chip comprises 275 K programmable logic units, 171 900 lookup tables, and a 17.6 Mb Block RAM. Further, both hardware and software programming functionalities are supported. Table 4 illustrates the performance parameters of the ZYNQ XC7Z035-FFG676-2I chip.

As shown in Fig.10, the image acquisition and processing circuit board is the smallest system of the ZYNQ XC7Z035-FFG676-2I chip, being mainly composed of the peripheral circuit that drives the ZYNQ XC7Z035-FFG676-2I chip to work normally and the external input and output interface circuit, including the main processor, the voltage conversion circuit, RS422/RS232 interface, the SD card interface, and the JTAG interface. The voltage conversion circuit converts the external input 5 V power supply into 3.3, 1.8, and 1.0 V, with the LTM4644IY chip being selected as the voltage conversion device. The voltage conversion chip works normally within the input voltage range of 2.375 V to 14 V of the external power supply, and supports the output voltage range of 0.6 V to 5.5 V. The program download and debugging are predominantly implemented through the JTAG interface, which consists of four signal wires, namely TCK, TDO, TMS, and TDI, corresponding to the clock, data output, mode selection, and data input signals, respectively. The RS232 interface adopts the MAX3232EUE chip as a signal converter to facilitate the transmission of RS232 signal between 3.0 V and 5.5 V power supplies with a maximum transmission rate of 1 Mb/s.

Table 4 Performance parameters of the ZYNQ XC7Z035-FFG676-2I chip

Parameter	Value
Processor	XC7Z035FFG676-2I, dual-core ARM Cortex-A9
Working frequency/MHz	800
FLASH/Mb	256
EMMC/GB	8
Logic unit/K	275
Number of lookup tables	171 900
Block RAM/Mb	17.6
System clock/MHz	33.333/100

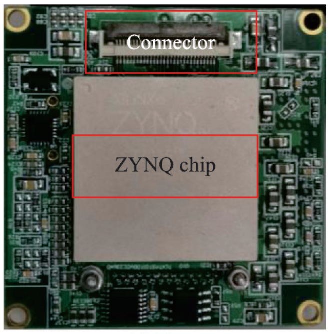

(a) Front

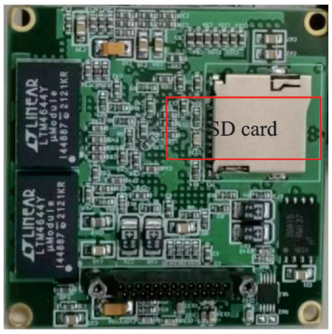

(b) Back

Fig.10 Hardware design of the image acquisition and processing circuit board

2 Ground Verification System Design

Fig.11 shows the overall architecture of the ground verification system, including module composition and data interaction. The ground verification system is mainly composed of dynamics simulation module, star map simulation module, optical simulator, GNC computer, and real-time monitoring display module. The blue line represents the physical signal and the red line the digital signal in Fig.11.

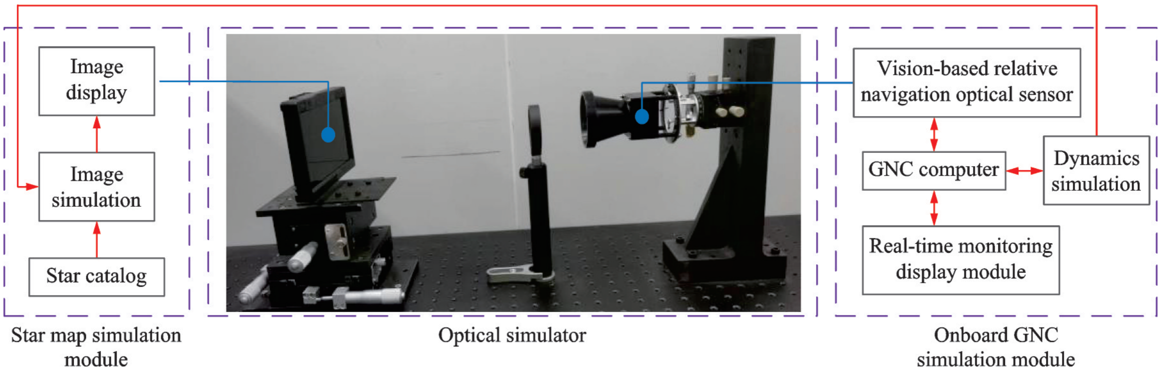

Fig.11 Overall architecture of the ground verification system

2.1 Dynamics simulation module design

The dynamics simulation module is created utilizing Simulink/xPC Target and comprises various simulation modules such as the time simulation module, attitude measurement and control simulation module, micro-thruster simulation module, chaser spacecraft and target spacecraft orbit recurrence module, and global navigation satellite system (GNSS) simulation module. The composition of the dynamics simulation module and data interaction with other modules are shown in Fig.12. The time simulation module is responsible for providing time input to the ground verification system. The chaser spacecraft and target spacecraft orbit recurrence module outputs the orbit data obtained through time recurrence to the star map simulation module. The GNSS simulation module outputs the simulated chaser spacecraft orbit data to the GNC computer, which in turn outputs the control force and torque to the micro-thruster simulation module and the attitude measurement and control simulation module.

Moreover, the high-precision orbit recurrence module includes a 21×21 order EGM08 gravity field model, a coordinate conversion model based on IAU 2000, an aerodynamic drag model based on NRLMSISE 2000 atmospheric density model, a third body perturbation model based on JPL DE436 ephemeris, and a solar pressure model.

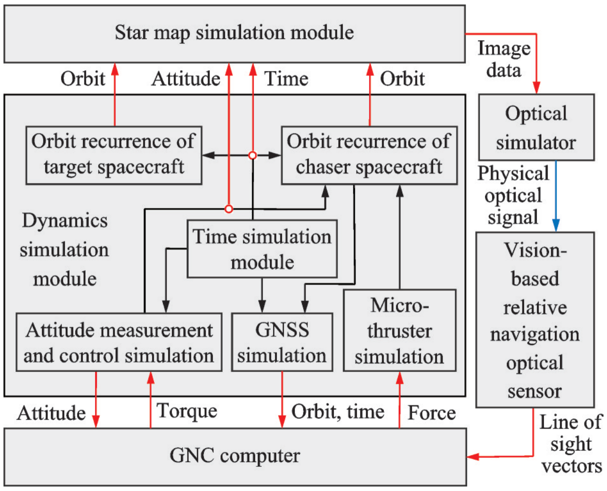

Fig.12 Data interaction relationship of the dynamics simulation module

2.2 Star map simulation module design

During autonomous proximity operations using vision-based relative navigation technology, its maximum distance can reach tens of kilometers, and its minimum distance may directly dock with the target spacecraft. In the presence of such a wide range of changing scenes, it is clearly impractical to validate the performances of the vision-based relative navigation systems by capturing images of actual model of the target spacecraft using the ground verification system. Such impracticality can be attributed to the unavailability of experimental sites spanning tens of kilometers, lack of darkroom environment, and the dynamic nature of the changing star field. Thus, the star map simulation design is adopted in the present study to provide input information for the research of autonomous recognition and tracking algorithms of space targets and the vision-based relative navigation algorithms, thereby promoting the design and verification of the entire autonomous proximity GNC system.

In the design of the star map simulation, the imaging parameters must be considered, such as resolution, focal length, pixel size, field angle, frame frequency, exposure time, gain, and noise of the vision-based relative navigation optical sensor, as well as the star background, attitude orientation and stability of the chaser spacecraft platform, orbital parameters of the chaser and target spacecraft, installation direction of the vision-based relative navigation optical sensor on the chaser spacecraft platform, sun illumination, surface materials of the target spacecraft, and size of the target spacecraft to generate simulated dynamic video images of the target spacecraft that change with time. The vision-based relative navigation optical sensor is used to take pictures of stars with different magnitudes in a clear and cloudless outdoor night sky scene, so as to ensure that the simulated background in the images closely resembles the real space environment. As shown in Fig.13, the actual brightness and size of stars with different magnitudes at different exposure times in images are obtained as reference data.

The main steps of star map simulation include:

(1) Projective transformation. Projection transformation refers to the calculation of the pixel coordinates in images according to the relative position vectors of the target spacecraft in the vision-based relative navigation optical sensor frame, the right ascension and declination information of stars, the attitude matrix of the chaser spacecraft, the installation matrix, and imaging parameters of the vision-based relative navigation optical sensor. The relative position vectors of the target spacecraft in the vision-based relative navigation optical sensor frame can be obtained by means of matrix transformation.

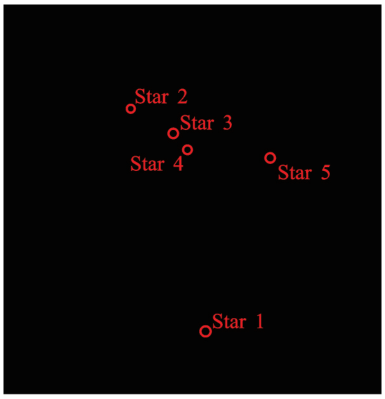

(a) Exposure time 1

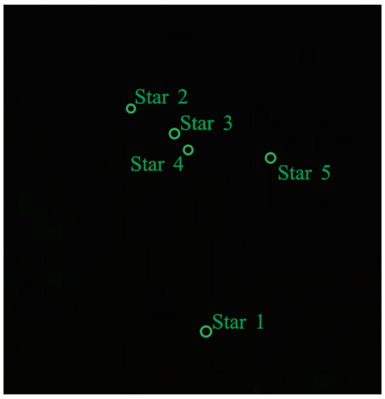

(b) Exposure time 2

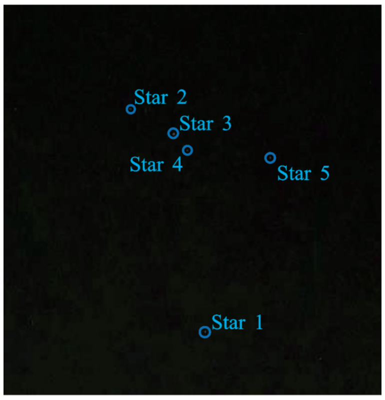

(c) Exposure time 3

Fig.13 Actual pictures taken by the optical sensor

By marking the position vectors of the origin of the J_{2000} geocentric inertial frame in the vision-based relative navigation optical sensor frame O_S-$X_S Y_S Z_S$ as $\boldsymbol{T}$, the position vectors $\boldsymbol{V}_t^S=[x_t^S, y_t^S, z_t^S]^T$ of the target spacecraft in the frame O_S-$X_S Y_S Z_S$ can be expressed as

$$\boldsymbol{V}_t^S=\boldsymbol{R}_{J_{2000}}^S \boldsymbol{V}_t^{J_{2000}}+\boldsymbol{T} \tag{1}$$

where $\boldsymbol{R}_{J_{2000}}^S$ represents the attitude conversion matrix from the J_{2000} geocentric inertial frame to the vision-based relative navigation optical sensor frame O_S-$X_S Y_S Z_S$; $\boldsymbol{V}_t^{J_{2000}}$ the position vectors of the target spacecraft in the J_{2000} geocentric inertial frame obtained by the high-precision orbit recurrence module of the target spacecraft.

For the vision-based relative navigation optical sensor with focal length of f, the coordinates $(x_{\mathrm{t}}^{\mathrm{R}}, y_{\mathrm{t}}^{\mathrm{R}})$ of the target spacecraft in the imaging frame O_{R}-xy can be expressed as

$$\begin{cases} \dfrac{x_{\mathrm{t}}^{\mathrm{R}}}{f} = \dfrac{x_{\mathrm{t}}^{\mathrm{S}}}{z_{\mathrm{t}}^{\mathrm{S}}} \\ \dfrac{y_{\mathrm{t}}^{\mathrm{R}}}{f} = \dfrac{y_{\mathrm{t}}^{\mathrm{S}}}{z_{\mathrm{t}}^{\mathrm{S}}} \end{cases} \tag{2}$$

Without considering the distortion of the imaging lens, according to the geometric relationship of the aperture imaging, by transforming the coordinate $(x_{\mathrm{t}}^{\mathrm{R}}, y_{\mathrm{t}}^{\mathrm{R}})$ to the pixel frame O_{P}-uv, and the pixel coordinate $(u_{\mathrm{t}}^{\mathrm{R}}, v_{\mathrm{t}}^{\mathrm{R}})$ of the target spacecraft in the images can be expressed as

$$\begin{cases} u_{\mathrm{t}}^{\mathrm{R}} = u_0 + \dfrac{x_{\mathrm{t}}^{\mathrm{R}}}{\mathrm{d}x} \\ v_{\mathrm{t}}^{\mathrm{R}} = v_0 + \dfrac{y_{\mathrm{t}}^{\mathrm{R}}}{\mathrm{d}y} \end{cases} \tag{3}$$

where u_0 and v_0 represent the center coordinates of the pixel plane; $\mathrm{d}x$ and $\mathrm{d}y$ the pixel size of the vision-based relative navigation optical sensor.

For the projection transformation of stars, since the stars are located at infinity under the J_{2000} geocentric inertial frame, the translation vector $\boldsymbol{T}$ in Eq.(1) can be ignored during the coordinate transformation. The unit direction vector $\boldsymbol{V}_{\mathrm{s}}^{J_{2000}} = [x_{\mathrm{s}}^{J_{2000}}, y_{\mathrm{s}}^{J_{2000}}, z_{\mathrm{s}}^{J_{2000}}]^{\mathrm{T}}$ of any star with right ascension of α_s and declination of β_{s} in the star catalog under the J_{2000} geocentric inertial frame can be expressed as

$$\begin{bmatrix} x_{\mathrm{s}}^{J_{2000}} \\ y_{\mathrm{s}}^{J_{2000}} \\ z_{\mathrm{s}}^{J_{2000}} \end{bmatrix} = \begin{bmatrix} \cos\beta_{\mathrm{s}} \cos\alpha_{\mathrm{s}} \\ \cos\beta_{\mathrm{s}} \sin\alpha_{\mathrm{s}} \\ \sin\beta_{\mathrm{s}} \end{bmatrix} \tag{4}$$

According to the calculation process of Eqs.(1—3), the pixel coordinates of stars in the images are obtained as $(u_{\mathrm{s}}^{\mathrm{P}}, v_{\mathrm{s}}^{\mathrm{P}})$.

(2) Gray value quantization. Magnitude is a unit of measurement commonly used in astronomy to indicate the brightness of stars. The magnitude scale is logarithmic, with higher magnitudes indicating fainter stars. In designing the star map simulation, the magnitude values listed in the star catalog need to be converted into corresponding gray values in the simulated images. Thus, the actual brightness and size of stars with different magnitudes in pictures taken by the vision-based relative navigation optical sensor are compared at different exposure times, as well as the simulation analysis results of the optical characteristics of the target spacecraft. Finally, the certain gray values are assigned to the target spacecraft and stars with different magnitudes.

(3) Image synthesis. In step (2), the gray values assigned to the target spacecraft and stars with different magnitudes cannot be directly used to fill the matrix in the pixel frame. Instead, the stars are projected onto the image plane and dispersed to multiple pixels, thus forming a light spot. The integral form of Gaussian distribution is closer to the real physical process, which can be expressed as

$$g(u_i, v_i) = \frac{\lambda}{2\pi\sigma^2} \int_{u_i - \frac{1}{2}}^{u_i + \frac{1}{2}} \int_{v_i - \frac{1}{2}}^{v_i + \frac{1}{2}} \exp\left[-\frac{(u - u_{\mathrm{t}}^{\mathrm{R}})^2 + (v - v_{\mathrm{t}}^{\mathrm{R}})^2}{2\sigma^2} \right] \mathrm{d}u \mathrm{d}v \tag{5}$$

where $(u_{\mathrm{t}}^{\mathrm{R}}, v_{\mathrm{t}}^{\mathrm{R}})$ is the projection coordinate calculated in Eq.(3); λ the energy gray scale coefficient; and σ the degree of defocus.

2.3 Optical simulator design

The optical simulator is the core component of this set of ground verification system for the hardware-in-the-loop testing of the vision-based relative navigation systems. The main function is to dynamically display the simulated star map in Section 2.2. The hardware composition of the designed optical simulator is described in this section, and the optical principle design of the optical simulator is introduced.

Figs.14—15 show the three-dimensional model and physical image of the optical simulator. The hardware composition of the optical simulator includes: (1) A precision three-axis guide rail, where each axis has a positioning accuracy of better than 0.05 mm; (2) a display screen with a resolution of

1 280×1 024; (3) an optical platform with a size specification of 300 mm×900 mm×13 mm; (4) a collimating lens; (5) an vision-based relative navigation optical sensor; (6) a real-time monitoring and display computer; (7) a dynamic image simulation computer; (8) an installation and adjustment structure of the display screen; (9) an installation and adjustment structure of the collimating lens; (10) a precision three-axis turntable, where each axis has a positioning accuracy of better than 0.005°; (11) an installation and adjustment structure of the vision-based relative navigation optical sensor. The performance parameters of the optical simulator are presented in Table 5.

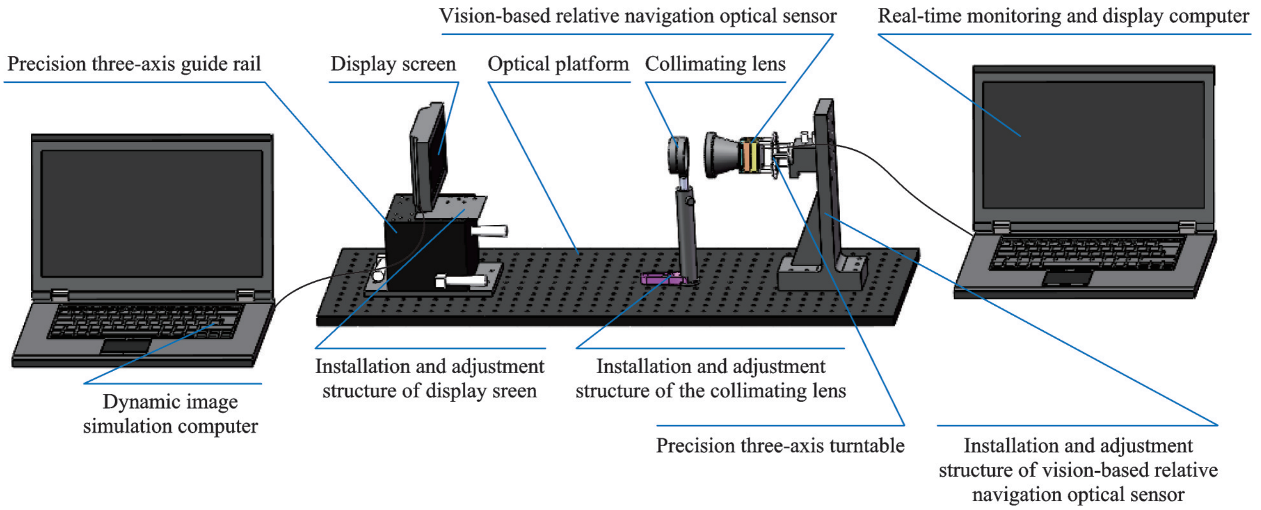

Fig.14 Three-dimensional model of the optical simulator

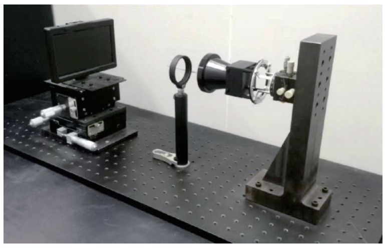

Fig.15 Physical image of the optical simulator

Table 5 Performance parameters of the optical simulator

Parameter	Value
Simulation magnitude range	More than 6 magnitude
Magnitude error	Less than ±0.3 magnitude
Inter-star angular distance error	Better than 30″
Star map update frequency	⩾10 Hz
Star map field of view	⩾15°×12°
Light source stability	Better than ±2%

Firstly, the collimating lens and the vision-based relative navigation optical sensor have to be installed coaxially, and the display screen has to be located at the focal plane of the collimating lens, as shown in Fig.16, meeting the following relationship

$$r = f_c \tag{6}$$

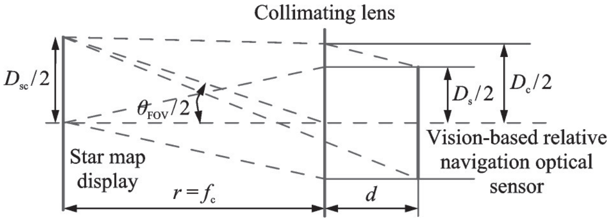

Fig.16 Optical schematic diagram of the optical simulator

Due to the equipped precision three-axis turntable and three-axis guide rail, the size of r can be adjusted, and the focal length f_c of the corresponding collimating lens needs to be changed accordingly. Such design requirement could be met by replacing the collimating lens with the corresponding focal length f_c, thereby realizing the adjustability of the optical simulator. Moreover, the field angle θ_{FOV} of the diagonal of the vision-based relative navigation optical sensor is suitable for the length D_{sc} of the diagonal of the display screen, which needs to meet the relationship shown as

$$f_c = \frac{D_{sc}}{2\tan(\theta_{FOV}/2)} \tag{7}$$

Moreover, the parameters of the collimating lens also include the minimum diameter D_c. In order to make the aperture of the vision-based relative navigation optical sensor fully illuminated by the collimating light from the edge light source of the display screen, D_c can be obtained as[26]

$$\frac{D_c}{2}=\frac{D_s}{2}+d\tan(\theta_{\text{FOV}}/2) \tag{8}$$

where D_s is the diameter of the imaging lens of the vision-based relative navigation optical sensor. In order to make D_c smaller, d should be as small as possible.

2. 4 GNC computer design

As the core component of the attitude and orbit control system, the GNC computer is a significant factor in the attitude and orbit control of the chaser spacecraft. By selecting high performance COTS devices, the GNC computer can fully meet the requirements of the attitude and orbit control system of the microsatellite platform. The hardware design of GNC computer is shown in Fig.17.

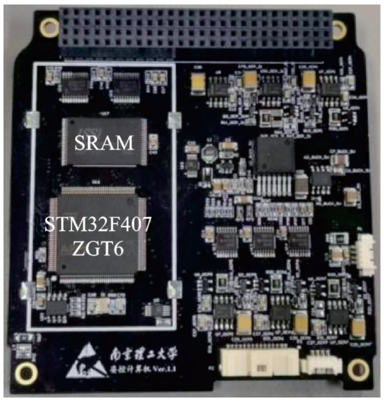

Fig.17 Hardware design of GNC computer

To ensure the efficient execution of various GNC algorithms on the microsatellite platform, the STM32F407ZGT6 chip is employed as the main processor of the GNC computer. The STM32F407 series processors are equipped with a 7-fold AHB bus matrix and a multi-channel DMA controller, facilitating data parallel processing and significantly enhancing the data operation rate. This series of processors provides the GNC system with 1 MB Flash, 192 KB SRAM, RC, PLL, and real-time clock. Moreover, the GNC computer also contains 15 communication interfaces, including six USART, three SPI, three I2C, two CAN, and one SDIO. In terms of peripheral devices, it also includes three 12-bit ADC, two 12-bit DAC, and 17 timers. The use of STM32F407 series processors has established the groundwork for practical implementation of the GNC system on the microsatellite platform. Table 6 shows performance parameters of the GNC computer.

Table 6 Performance parameters of the GNC computer

Parameter	Value
Supply voltage/V	7.4/5/3.3
Processor	High performance ARM Cortex-M4, 32-bit RISC kernel
I2C interface	Three-way I2C bus extension
Debugging interface	SWD pattern
Other interfaces	SPI/PWM/ADC/RS232

3 Experimental Testing and Result Analysis

3. 1 Star map simulation testing

The star map simulation design is performed using MATLAB R2018a. According to the hardware performances of the vision-based relative navigation optical sensor, the stars with a brightness above 6 magnitude can be recognized, and those with a brightness below 6 magnitude are ignored in the star map simulation. When simulating the star map, the assumption is that the mean magnitude error is 0 and the variance is 0.01 Gaussian white noise. The image background is equivalent to the brightness of 10 magnitude, and the exposure coefficient of the vision-based relative navigation optical sensor is selected as 1. A further assumption is that the installation direction of the vision-based relative navigation optical sensor is aligned with the chaser spacecraft body frame, and the chaser spacecraft platform is in a three-axis stable state. The main simulation parameters in the process of the star map simulation are shown in Table 7. The simulated images are shown in Figs.18—19, where Fig.18 is the simulated image without adding device noise, and Fig.19 the simulated image with adding device noise.

Table 7 Main simulation parameters during star map simulation

Parameter	Value
Initial orbital elements of target spacecraft	$[6\,878.137\ \text{km},\ 0,\ 5°,\ 120°,\ 0°,\ 50°]^{\mathrm{T}}$
Initial orbital elements of chaser spacecraft	$[6\,878.137\ \text{km},\ 7.3\times10^{-5},\ 4.996°,\ 120°,\ 0°,\ 49.757°]^{\mathrm{T}}$
Standard deviation of measurement error of optical sensor	$\sigma_{\alpha}=\sigma_{\varepsilon}=18''$
Standard deviation of measurement deviation of optical sensor	$\sigma_{b,\alpha}=\sigma_{b,\varepsilon}=5''$
Standard deviation of attitude determination error	$(\sigma_{\text{att, off-axis}},\ \sigma_{\text{att, roll}})=(6'',\ 40'')$

Fig.18 Simulated image without adding device noise

Fig.19 Simulated image with adding device noise

The system distortion of the optical simulator is geometrically calibrated using the method proposed in Ref.[27] to improve the angular accuracy of star centroids in simulated images. Fig.20 shows the comparison between positions of stars before and after geometrical calibration. The inter-star angular distance before and after geometrical calibration is measured by the theodolite, and the accuracy of the theodolite is better than 2″. The results show that the average error of the inter-star angular distance is 5.71″(3σ), meeting the index requirements of optical simulator with inter-star angular distance error better than 30″. The average errors of inter-star angular distance and target spacecraft centroid before and after geometrical calibration are shown in Table 8. The calculation equation of the average error m_{a} of inter-star angular distance is expressed as

$$m_{\mathrm{a}}=\frac{1}{N}\sum_{i=1}^{N}(\bar{m}_i-\tilde{m}_i) \tag{9}$$

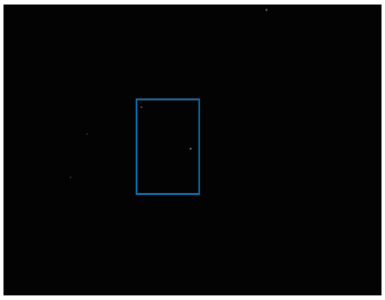

(a) Before geometrical calibration

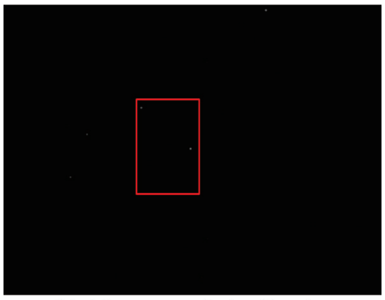

(b) After geometrical calibration

Fig.20 Comparison between positions of stars before and after geometrical calibration

Table 8 Average error of inter-star angular distance and target spacecraft centroid

Parameter	Before geometrical calibration	After geometrical calibration
Inter-star angular distance/(″)	18.78	5.71
Target spacecraft centroid azimuth/(″)	21.52	8.87
Target spacecraft centroid elevation/(″)	25.45	9.36

Further, in addition to considering the background of stars, star map simulation is also conducted at different inter-satellite distances by combining the real images in a fully-real ground simulation experiment scene. The scene involves imaging a reduced scale model of the target spacecraft made of real materials under real illumination conditions simulated by the sun simulator, as depicted in Fig.21. The sun simulator uses xenon lamp as the light source with the irradiation nonuniformity of less than 3%, and the irradiation intensity is adjustable in the range of 1 000—4 000 W/m^2. The star map simulation results are shown in Fig.22. Finally, the positioning accuracy of the target spacecraft centroid at different inter-satellite distances is analyzed, whose results are shown in Table 9. An observation can be made from Table 9 that the positioning accuracy of the target spacecraft centroid will decline with the decrease in inter-satellite distance.

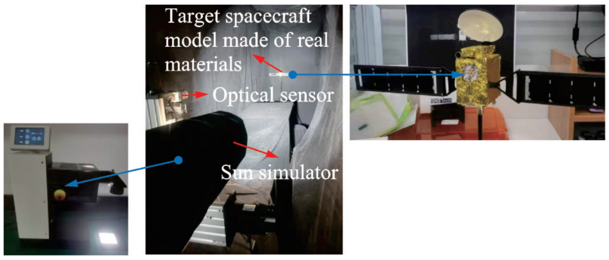

Fig.21 Fully-real ground simulation experiment scene

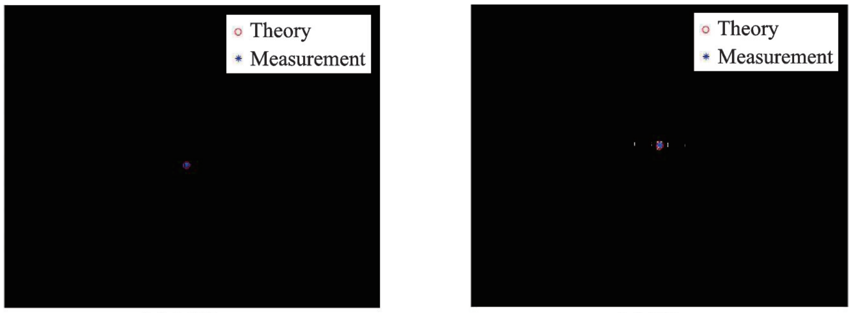

(a) 1 278 m (b) 511 m

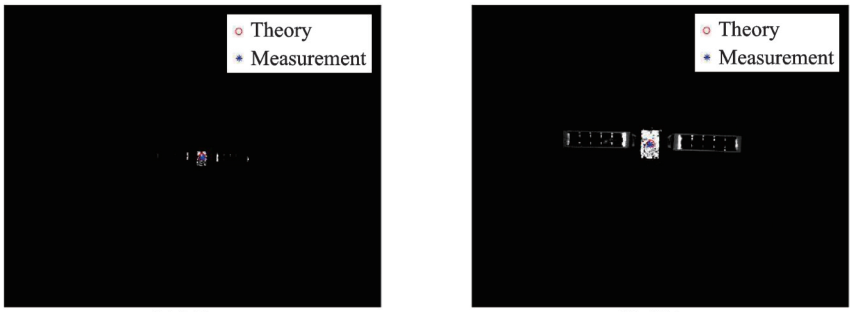

(c) 383 m (d) 206 m

Fig.22 Star map simulation at different inter-satellite distances

Table 9 Positioning accuracy of target spacecraft centroid

Inter-satellite distance/m	Centroid theoretical value/pixel	Centroid measured value/pixel	Centroid error absolute value/pixel
206	(607, 470)	(605.2, 472.7)	(1.8, 2.7)
383	(671.5, 515)	(672.6, 516.9)	(1.1, 1.9)
511	(640.5, 478)	(641.3, 476.8)	(0.8, 1.2)
1 278	(618, 543)	(618.5, 542.3)	(0.5, 0.7)

3.2 Hardware-in-the-loop testing of vision-based relative navigation algorithm

The designed vision-based relative navigation optical sensor and the angles-only navigation algorithms proposed by authors in previous research[28] are tested on the ground verification system. The general architecture of the angles-only navigation algorithms is shown in Fig.23. Firstly, the vision-based relative navigation optical sensor captures the simulated star field, which includes the target spacecraft displayed on the screen. Next, the acquired images are preprocessed, and the centroids of all stars are extracted. The star catalog and satellite attitude information are then combined to eliminate the cen-

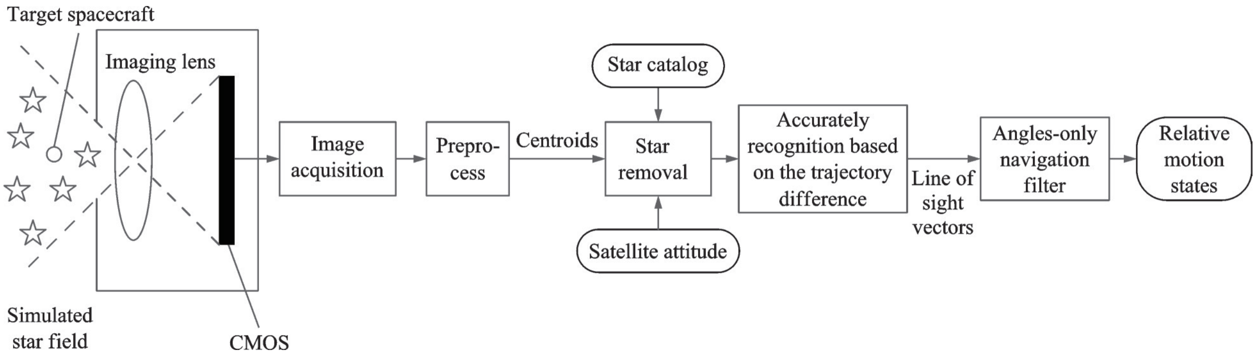

Fig.23 General architecture of angles-only navigation algorithms

troids of non-target spacecraft. The target spacecraft is subsequently recognized accurately based on the trajectory difference[29]. Finally, to obtain the relative motion states between the chaser spacecraft and the target spacecraft, the extracted line-of-sight vectors of the target spacecraft are substituted into the angles-only navigation filter.

Fig.24 shows the schematic diagram of star classification results, including target spacecraft, star, unrecognized object, and camera noise. Table 10 shows statistical results of target spacecraft recognition success rate before and after geometrical calibration. An observation can be made from Table 10 that the target spacecraft recognition success rate before and after geometrical calibration is greater than 96%, and the target spacecraft recognition success rate after geometrical calibration is better than that before.

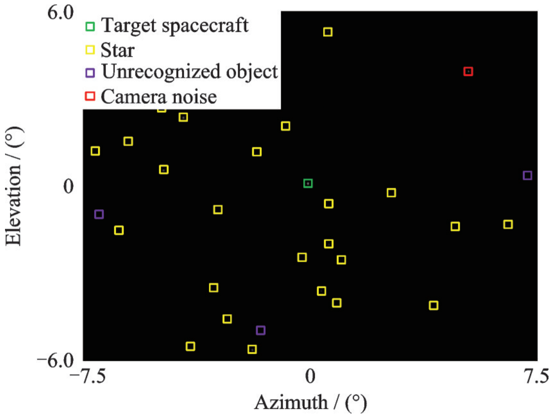

Fig.24 Schematic diagram of star classification results

Table 10 Target spacecraft recognition success rate

Scenario	Number of frames of the target spacecraft recognized	Number of frames of the target spacecraft unrecognized	Total frames	Recognition success rate/%
Before geometrical calibration	2 887	113	3 000	96.23
After geometrical calibration	2 956	44	3 000	98.53

In a typical orbital scenario, the hardware-in-the-loop testing of the angles-only navigation algorithms under the rectilinear/curvilinear state relative dynamics model proposed by the authors in previous research[28] is conducted on the ground verification system. Fig.25 shows experimental diagram of the ground verification system, for which the experimental devices includes an optical simulator, a GNC computer, a dynamics simulation computer, an vision-based relative navigation optical sensor, and a real-time monitoring display module.

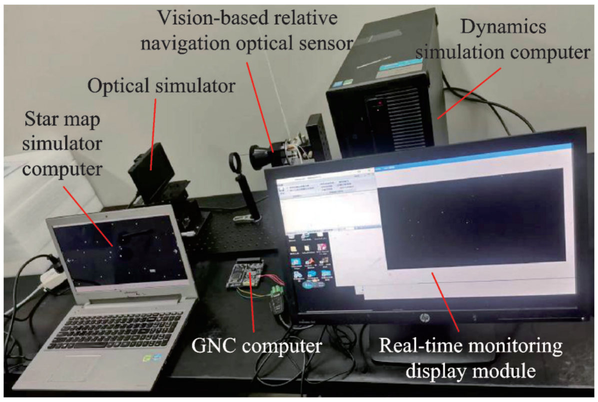

Fig.25 Experimental diagram of the ground verification system

Figs.26—28 show the hardware-in-the-loop testing results of the angles-only navigation algorithms under the rectilinear/curvilinear state relative dynamics model. Fig.26 shows the estimated relative motion trajectories of the angles-only navigation algorithm under the rectilinear state relative dynamics model, Fig.27 shows the estimation errors of the angles-only navigation algorithm under the rectilinear state relative dynamics model before and after geometrical calibration, and Fig.28 shows the estimation errors of the angles-only navigation algorithm under the curvilinear state relative dynamics model before and after geometrical calibration.

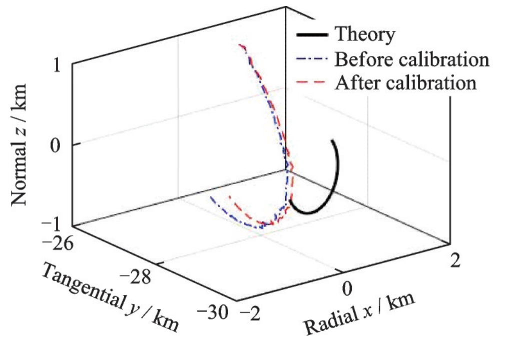

Fig.26 Estimated relative motion trajectories of the angles-only navigation algorithm

An observation can be made from Figs.27—28 that the angles-only navigation filter under the rectilinear/ curvilinear state relative dynamics model can

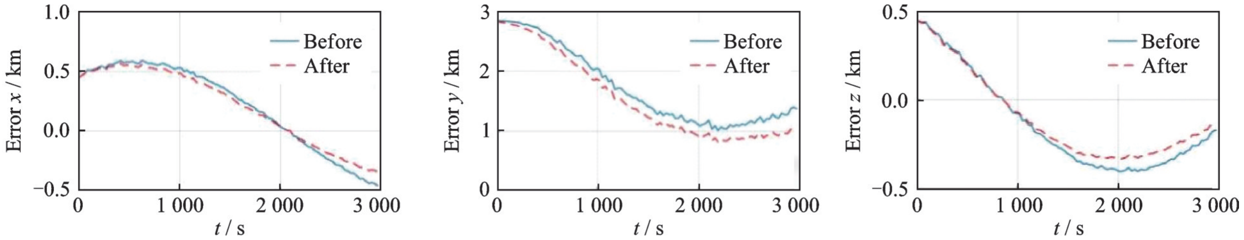

(a) Estimation error of x (b) Estimation error of y (c) Estimation error of z

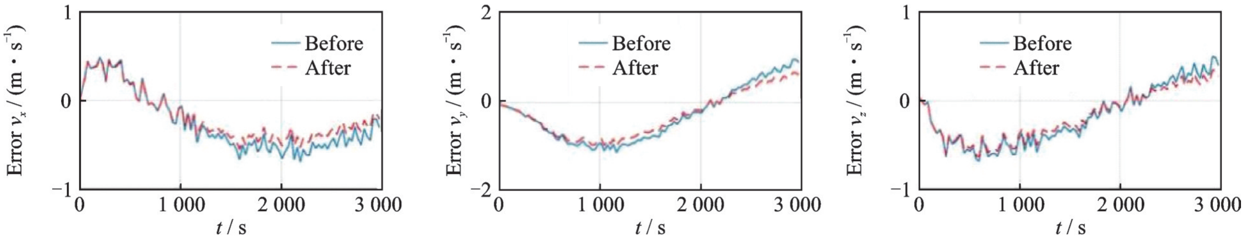

(d) Estimation error of v_x (e) Estimation error of v_y (f) Estimation error of v_z

Fig.27 Estimation errors of the angles-only navigation algorithm under the rectilinear state relative dynamics model

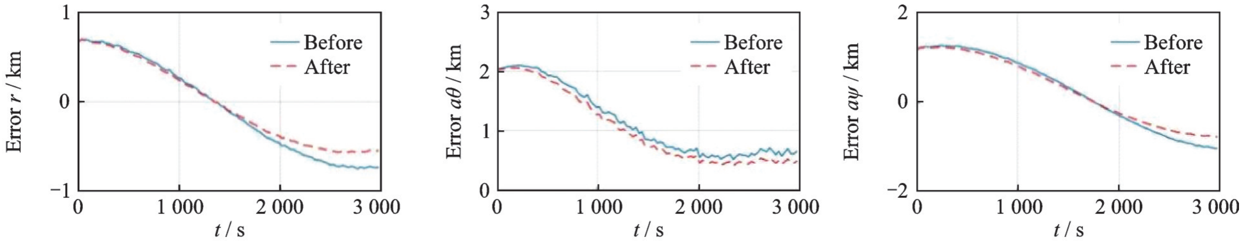

(a) Estimation error of r (b) Estimation error of $a\theta$ (c) Estimation error of $a\psi$

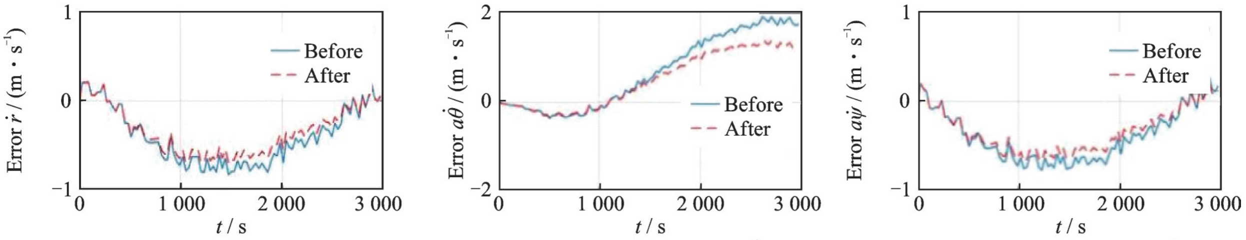

(d) Estimation error of $\dot{r}$ (e) Estimation error of $a\dot{\theta}$ (f) Estimation error of $a\dot{\psi}$

Fig.28 Estimation errors of the angles-only navigation algorithm under the curvilinear state relative dynamics model converge slowly, but the angles-only navigation filter under the rectilinear state relative dynamics model has poor observability, resulting in the poor convergence of the angles-only navigation filter. However, the angles-only navigation filter under the curvilinear state relative dynamics model has better convergence and higher filtering accuracy, demonstrating that the angles-only navigation system under the curvilinear state relative dynamics model has better observability. Further, the accuracy of relative position at terminal time is improved by 25.5% after geometrical calibration compared to before, while the accuracy of relative speed at terminal time is improved by 31.3% after geometrical calibration compared to before. Thus, the geometrical calibration of optical simulator can improve the performances of the angles-only navigation filter, and also prove that the optical simulator after geometrical calibration can meet the requirements of the hardware-in-the-loop testing of the vision-based relative navigation systems. Moreover, the estimation errors of the angles-only navigation filter obtained from experimental testing are larger than those of numerical simulation. This is due to the inability to eliminate device installation errors and lens distortion errors in experimental testing system. Therefore, there is a problem of over idealization in the setting of certain parameters in numerical simulation.

4 Conclusions

An vision-based relative navigation optical sensor suitable for the microsatellite platform is designed, including the detailed design of the imaging lens, lens hood, electronic warehouse, imaging circuit board, and image acquisition and processing circuit board. A set of ground verification system for the hardware-in-the-loop testing of the vision-based relative navigation systems is built, including the detailed design of the dynamic simulation module, star map simulation module, optical simulator, and GNC computer. The designed vision-based relative navigation optical sensor and the proposed angles-only navigation algorithms are tested on the ground verification system. The results verify that the optical simulator after geometrical calibration can meet the requirements of the hardware-in-the-loop testing of the vision-based relative navigation systems. As such, the present study provides an effective experimental method and a system-wide hardware design solution for the engineering application of the vision-based relative navigation technology on the microsatellite platform.

Subsequent improvements can be made to the design of optical simulator by adding another collimating lens to achieve the design of variable magnification optical simulator, so as to meet needs of different scenarios.

References

[1] AGLIETTI G S, TAYLOR B, FELLOWES S, et al. The active space debris removal mission RemoveDebris. Part 2: In orbit operations[J]. Acta Astronautica, 2020, 168: 310-322.

[2] NIKOLICHEV I A, SVOTINA V V. Contactless space debris removal from the geostationary orbit protected region[J]. Acta Astronautica, 2024, 215: 523-533.

[3] SEARS P J, HO K. Impact evaluation of in-space additive manufacturing and recycling technologies for on-orbit servicing[J]. Journal of Spacecraft and Rockets, 2018, 55(6): 1498-1508.

[4] ZHENG M Y, ZHANG Y L, FAN L. Retrieval dynamics and control for approach of tethered on-orbit service satellite[J]. Advances in Space Research, 2023, 71(12): 4995-5006.

[5] SHE Y C, LI S, DU B, et al. On-orbit assembly mission planning considering topological constraint and attitude disturbance[J]. Acta Astronautica, 2018, 152: 692-704.

[6] ZHU Z H, GUO Y. Adaptive coordinated attitude control for spacecraft formation with saturating actuators and unknown inertia[J]. Journal of the Franklin Institute, 2019, 356(2): 1021-1037.

[7] WANG Z F, TIAN J R, FU J. Fuel optimization schemes for formation reconfiguration in satellite formation flying[J]. Advances in Space Research, 2023, 72(5): 1496-1508.

[8] NING Xiaolin, CHAO Wen, YANG Yuqing. A method against ephemeris error in deep space celestial angle measurement navigation[J]. Journal of Astro-

nautics, 2019, 40(12): 1412-1421. (in Chinese)

[9] WAN Weixing, WEI Yong, GUO Zhengtang, et al. Toward a power of planetary science from a gaint of deep space exploration[J]. Bulletin of Chinese Academy of Science, 2019, 34(7): 748-755.

[10] YANG Tao, ZHANG Weihua, GIANMARCO R, et al. Investigation of application of motion camouflage on space attack and defence[J]. Journal of Astronautics, 2010, 31(8): 1964-1969. (in Chinese)

[11] ZHANG S Q, WANG Z G, RAN L S. Space rendezvous and docking measurement techniques and engineering applications[M]. Beijing: China Aerospace Press, 2005.

[12] GRZYMISCH J, FICHTER W. Observability criteria and unobservable maneuvers for in-orbit bearings-only navigation[J]. Journal of Guidance, Control, and Dynamics, 2014, 37(4): 1250-1259.

[13] GONG B C, LI W, LI S, et al. Angles-only initial relative orbit determination algorithm for noncooperative spacecraft proximity operations[J]. Astrodynamics, 2018, 2(3): 217-231.

[14] SULLIVAN J, KOENIG A W, D'AMICO S. Improved maneuver-free approach to angles-only navigation for space rendezvous[C]//Proceedings of the 26th AAS/AIAA Space Flight Mechanics Meeting. Napa, CA: AIAA, 2016.

[15] ARDAENS J S, GAIAS G. Flight demonstration of spaceborne real-time angles-only navigation to a noncooperative target in low Earth orbit[J]. Acta Astronautica, 2018, 153: 367-382.

[16] WOFFINDEN D C, GELLER D K. Navigating the road to autonomous orbital rendezvous[J]. Journal of Spacecraft and Rockets, 2007, 44(4): 898-909.

[17] GELLER D K, LOVELL T A. Angles-only initial relative orbit determination performance analysis using cylindrical coordinates[J]. Journal of the Astronautical Sciences, 2017, 64(1): 72-96.

[18] SHENG Z C, GUO Y F, XUE A K. Multi-sensor multi-target bearing-only tracking with signal time delay[J]. Signal Image and Video Processing, 2023, 17(8): 4495-4502.

[19] CHEN T, XU S J. Double line-of-sight measuring relative navigation for spacecraft autonomous rendezvous[J]. Acta Astronautica, 2010, 67(1/2): 122-134.

[20] PEREZ A C, GELLER D K, LOVELL T A. Non-iterative angles-only initial relative orbit determination with J_2 perturbations[J]. Acta Astronautica, 2018, 151: 146-159.

[21] ARDAENS J S, GAIAS G. A numerical approach to the problem of angles-only initial relative orbit determination in low Earth orbit[J]. Advances in Space Research, 2019, 63(12): 3884-3899.

[22] PI J, BANG H. Trajectory design for improving observability of angles-only relative navigation between two satellites[J]. Journal of the Astronautical Sciences, 2014, 61(4): 1-22.

[23] FRANQUIZ F J, MUNOZ J D, UDREA B, et al. Optimal range observability maneuvers of a spacecraft formation using angles-only navigation[J]. Acta Astronautica, 2018, 153: 337-348.

[24] GONG B C, LI S, YANG Y, et al. Maneuver-free approach to range-only initial relative orbit determination for spacecraft proximity operations[J]. Acta Astronautica, 2019, 163: 87-95.

[25] LI Yang, LIAO Zhibo, MU Shengbo, et al. Stray light suppressing technique and simulation for star sensor[J]. Journal of Beijing University of Aeronautics and Astronautics, 2016, 42(12): 2620-2624. (in Chinese)

[26] RUFINO G, MOCCIA A. Laboratory test system for performance evaluation of advanced star sensors[J]. Journal of Guidance, Control, and Dynamics, 2002, 25(2): 200-208.

[27] BEIERLE C, D'AMICO S. Variable-magnification optical stimulator for training and validation of spaceborne vision-based navigation[J]. Journal of Spacecraft and Rockets, 2019, 56(4): 1060-1072.

[28] DU R H, LIAO W H, ZHANG X. Non-linear dynamics method to angles-only navigation for non-cooperative rendezvous of spacecraft[J]. Transactions of Nanjing University of Aeronautics and Astronautics, 2022, 39(4): 400-414.

[29] DU Ronghua, ZHANG Xiang, WANG Ning, et al. Research on autonomous detection and tracking method for rendezvous and proximity of an uncooperative target[J]. Journal of Astronautics, 2021, 42(5): 621-633. (in Chinese)

Acknowledgements This work was supported in part by the Doctoral Initiation Fund of Nanchang Hangkong University (No.EA202403107), and Jiangxi Province Early Career Youth Science and Technology Talent Training Project (No.CK202403509).

Author

The first/corresponding author Dr. **DU Ronghua** received the B.S. degree in mechanical design, manufacturing and automation from School of Mechanical Engineering, Nanjing University of Science and Technology, Nanjing, China, in 2017 and the Ph.D. degree in mechanical engineering from School of Mechanical Engineering, Nanjing University of Science and Technology, Nanjing, China, in 2023. He is currently the lecturer with School of Aviation Manufacturing and Mechanical Engineering, Nanchang Hangkong University, Nanchang, China. His research interests include satellite attitude determination, vision-based relative navigation, guidance navigation and control, and angles-only relative navigation.

Author contributions Dr. **DU Ronghua** designed the study, complied the models, conducted the experimental analysis, interpreted experimental results, and wrote the manuscript. Prof. **LIAO Wenhe** contributed to data for hardware-in-the-loop testing and result analysis. Prof. **ZHANG Xiang** contributed to the discussion and background of the study. All authors commented on the manuscript draft and approved the submission.

Competing interests The authors declare no competing interests.

(Production Editor: WANG Jing)

基于视觉的微小卫星相对导航系统设计与地面验证

杜荣华[1]，廖文和[2]，张　翔[2]
(1.南昌航空大学航空制造与机械工程学院,南昌 330063,中国;
2.南京理工大学微纳卫星研究中心,南京 210094,中国)

摘要:介绍了基于视觉的微小卫星相对导航系统设计和地面验证,为在微小卫星平台上实施视觉导航技术提供了全面的硬件设计解决方案和稳健的实验验证方法。首先,设计了一种低功耗、轻量化、高性能的视觉相对导航光学传感器;然后,设计了一套地面验证系统,以用于视觉相对导航系统硬件在环测试;最后,在地面验证系统上对设计的视觉相对导航光学传感器和提出的仅测角导航算法进行了实验测试,结果验证了几何校准后的光学模拟器能够满足视觉相对导航系统硬件在环测试要求。根据实验测试结果,与几何校准前的光学模拟器相比,仅测角导航滤波器在终端时刻的相对位置精度提高了25.5%,相对速度精度提高了31.3%。

关键词:微小卫星;视觉相对导航;光学模拟器;地面验证;仅测角导航